

Beyond fixed thresholds: optimizing summaries of wearable device data via piecewise linearization of quantile functions

Junyoung Park, Neo Kok, Irina Gaynanova

Department of Biostatistics, University of Michigan, Ann Arbor, Michigan, USA

Abstract

Wearable devices, such as actigraphy monitors and continuous glucose monitors (CGMs), capture high-frequency data, which are often summarized by the percentages of time spent within fixed thresholds. For example, actigraphy data are categorized into sedentary, light, and moderate-to-vigorous activity, while CGM data are divided into hypoglycemia, normoglycemia, and hyperglycemia based on a standard glucose range of 70–180 mg/dL. Although scientific and clinical guidelines inform the choice of thresholds, it remains unclear whether this choice is optimal and whether the same thresholds should be applied across different populations. In this work, we define threshold optimality with loss functions that quantify discrepancies between the full empirical distributions of wearable device measurements and their discretizations based on specific thresholds. We introduce two loss functions: one that aims to accurately reconstruct the original distributions and another that preserves the pairwise sample distances. Using the Wasserstein distance as the base measure, we reformulate the loss minimization as optimal piecewise linearization of quantile functions. We solve this optimization via stepwise algorithms and differential evolution. We also formulate semi-supervised approaches where some thresholds are predefined based on scientific rationale. Applications to CGM data from two distinct populations—individuals with type 1 diabetes and those with normal glycemic control—demonstrate that data-driven thresholds vary by population and improve discriminative power over fixed thresholds.

Keywords: Amalgamation; Continuous glucose monitoring (CGM); Histogram; Time-in-Range (TIR); Wasserstein distance.

1 Introduction

Advances in wearable device technology have opened up new avenues for healthcare research by enabling real-time monitoring of physiological variables outside traditional clinical settings. Devices such as actigraphy monitors and continuous glucose monitors (CGMs) generate high-frequency, individualized time series data that promise to offer new insights into a wearer’s health status. Actigraphy monitors capture detailed physical activity patterns (Fishman et al., 2016; Matabuena and Petersen, 2023; Ghosal and Matabuena, 2024), while CGMs provide critical data for diabetes management by recording interstitial glucose levels at frequent time intervals (Broll et al., 2021; Battelino et al., 2023). With continued improvements in convenience and cost-effectiveness, wearable devices are being rapidly adopted in both clinical and personal health monitoring. Consequently, their data have significant potential for enhancing our understanding of human health and disease.

Despite this promise, wearable device data pose substantial analytical challenges due to their high measurement frequency and varying monitoring durations. Thus, researchers commonly summarize these data using fixed thresholds. Actigraphy data, which record movement intensities in activity count per minute, are often summarized into time spent in sedentary, light, moderate, and vigorous activity categories defined, for example, by thresholds at 100, 200, and 5999 activity counts (Troiano et al., 2008; Fishman et al., 2016). In diabetes studies, CGM data are similarly summarized via Time-in-Range (TIR) metrics, which indicate the percentage of time glucose levels fall within ranges defined by established consensus thresholds: less than 54 mg/dL, 54–69 mg/dL, 70–180 mg/dL, 181–250 mg/dL, and above 250 mg/dL (Battelino et al., 2019, 2023). These thresholds are determined based on scientific and clinical reasoning, resulting in parsimonious and interpretable data summaries.

Nonetheless, using fixed thresholds has several limitations. Threshold-based summaries inevitably discard fine-grained information captured by wearable devices. Furthermore, they may not reflect physiological differences across diverse populations (e.g., age, race, sex, and health conditions), potentially leading to biased or oversimplified interpretations. In the context of CGM data, it is unclear whether the existing thresholds are optimal and whether the same glycemic thresholds are appropriate for individuals with type 2 diabetes and those with type 1 diabetes. Notably, Katta et al. (2024) recently highlighted that adjusting CGM thresholds, such as altering the “healthy” glucose range from 70–180 mg/dL to 70–140 mg/dL, can lead to substantially different interpretations of treatment effects, underscoring the importance of selecting the “right” thresholds.

An emerging alternative to fixed threshold-based summaries is representing wearable device data as entire *distributions*. Distributional representations continuously extend threshold-based summaries by encoding the time spent within each infinitesimal range across the entire domain. This approach thus maintains greater data granularity compared to the conventional summaries, resulting in improved analytic performance (Matabuena et al., 2021; Katta et al., 2024). However, distributional representations may be challenging to interpret and communicate in clinical settings. In contrast, threshold-based metrics provide simple, interpretable scalars that can be readily utilized in clinical tasks, such as setting treatment goals.

To balance the interpretability of fixed threshold-based summaries and the precision of distributional representations, we propose a framework for deriving data-dependent optimal thresholds. Inspired by the concept of *amalgamation* from compositional data analysis (Aitchison, 1982; Li et al., 2022), which reduces dimension by merging compositional variables, we view threshold selection as amalgamating adjacent bins in a histogram of the full empirical distribution. Figure 1a illustrates this transformation of an empirical CGM distribution into a coarser histogram by amalgamating intermediate bins between selected thresholds. We then quantify threshold optimality using two loss functions: one measures the discrepancy between the original and amalgamated distributions, while the other preserves pairwise distances between distributions.

Specifically, we use the Wasserstein distance as our primary discrepancy measure between histograms, which quantifies the optimal transport cost between distributions (Villani, 2003). This metric effectively captures the geometry of the underlying domain of distributions and has been successfully applied to distributional data and histograms (Irpino and Verde, 2006; Park et al., 2019). By leveraging the quantile-based computation of the Wasserstein distance for univariate distributions, we demonstrate a connection between histogram amalgamation and linear interpolation of quantiles (Figure 1b), allowing us to reinterpret threshold selection as *optimal piecewise*

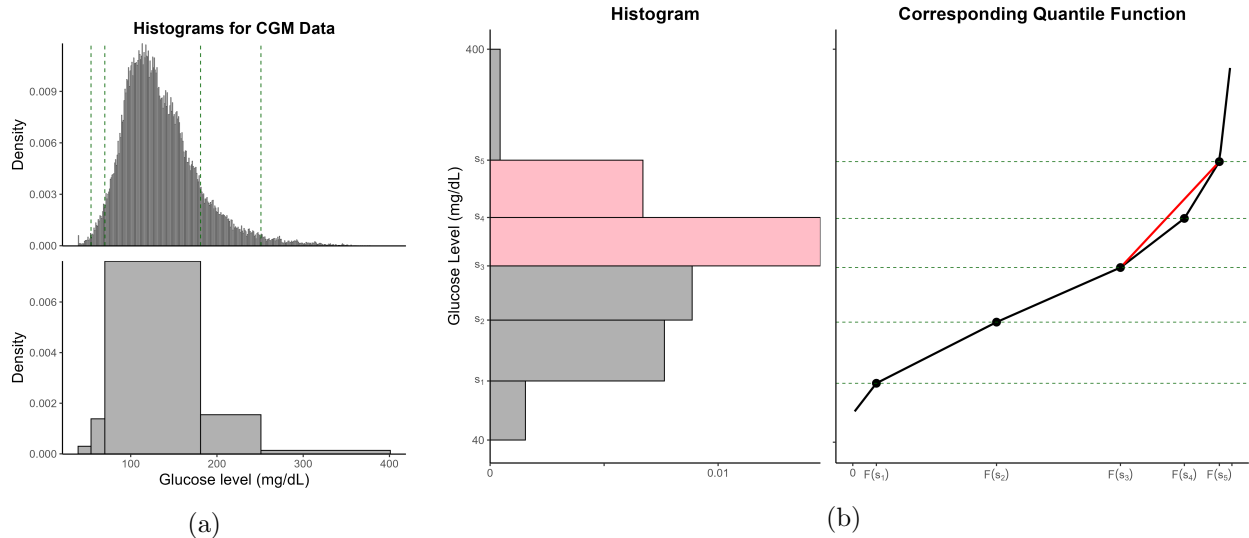


Figure 1: (a) Histograms of CGM measurements from a type 1 diabetes patient from [Brown et al. \(2019\)](#). The top panel shows the full empirical distribution using a fixed bin width of 1 mg/dL, while the bottom panel amalgamates intermediate bins of four consensus thresholds—54, 70, 181, and 251 mg/dL—to create a coarser summary. (b) Illustration of the quantile function (right) of a histogram (left) and their amalgamations. The amalgamation of red bins corresponds to the coarser linearization of the quantile function, depicted by the red line.

linearization of quantile functions. This perspective enables the efficient computation of the objective function of threshold optimization. Since it is a discrete optimization with a large search space, we propose two practical approaches: stepwise amalgamations and global optimization with continuous relaxation, solved using differential evolution ([Das and Suganthan, 2011](#)). Furthermore, our methods extend to a semi-supervised setting, which allows fixing certain clinically crucial thresholds while optimizing additional thresholds to better capture the distributional structures.

The proposed approach to data-driven thresholds fundamentally differs from the classical histogram binning methods ([Freedman and Diaconis, 1981](#); [Knuth, 2019](#)) and piecewise linearization ([Natali and Pinto, 2009](#)); these problems focus on a single distribution or function, whereas our work focuses on deriving optimal thresholds that apply to *multiple distributions*. Additionally, while we adopt the concept of amalgamation from compositional data analysis, our approach goes beyond the purely compositional viewpoint often considered in actigraphy studies ([Janssen et al., 2020](#)) by accounting for the inherent orderings of wearable device measurements. There are related recent works on data-driven thresholds by [Banker and Song \(2023\)](#) and [Banker et al. \(2024\)](#), building on the supervised, scalar-on-function regression model with distributional predictors. However, their data-driven thresholds rely on the presence of continuous response variables, which limits their generalizability and introduces potential risks of overfitting. In contrast, our unsupervised framework uses only distributional characteristics of the data to derive thresholds and optimize TIR summaries, ensuring broad applicability without dependence on external response variables.

In summary, our main contributions are: (1) a formulation of data-driven thresholds for optimal summaries of wearable device data, (2) a novel method for selecting thresholds with the piecewise-linear approximation of quantiles, and (3) two practical estimation approaches, stepwise algorithms

and a global optimization with differential evolution, which can also accommodate semi-supervised scenarios. Our analyses of real CGM data reveal that data-driven thresholds capture considerable differences between individuals without diabetes and those with type 1 diabetes, suggesting potential improvements over the consensus thresholds for CGM data.

2 Optimal data-driven thresholds

This section formalizes the concept of optimal data-driven thresholds based on the compositional structure of histogram data.

Our motivating example is CGM data, where glucose levels are recorded as integers from 40 to 400 mg/dL. The empirical distributional representation of these measurements for each individual is captured by a high-resolution histogram h , where each bin corresponds to a specific glucose value. Let $h(i)$ be the proportion of measurements at integer glucose level i , then histogram h corresponds to a compositional vector:

$$\mathbf{x} = (h(40), h(41), \dots, h(400)) \in \Delta^{360},$$

where $\Delta^p = \{(z_0, \dots, z_p) \in \mathbb{R}_{\geq 0}^{p+1} \mid \sum_{i=0}^p z_i = 1\}$ is the p -dimensional probability simplex.

Using fixed consensus CGM thresholds of 54, 70, 181, and 251 mg/dL (Battelino et al., 2023), the corresponding summary of original histogram h yields reduced compositional representation:

$$\left(\sum_{i=40}^{53} h(i), \sum_{i=54}^{69} h(i), \sum_{i=70}^{180} h(i), \sum_{i=181}^{250} h(i), \sum_{i=251}^{400} h(i) \right) \in \Delta^4,$$

where each component indicates Time-in-Range (TIR) proportions for 40–53, 54–69, 70–180, 181–250, and 251–400 mg/dL, respectively. This process aligns with amalgamation in compositional data analysis (Aitchison, 1982), with the additional constraint of merging only neighboring components to reflect the natural ordering of glucose values (Figure 1a). Thus, a threshold-based summary inherently performs dimension reduction on the compositional level, so we can formulate the optimal threshold problem as a dimension reduction problem: reducing the number of bins while aiming to preserve the key characteristics of the original histogram h .

To generalize this idea, let h_1, \dots, h_n denote histogram data on a bounded interval $\Omega = [a, b]$ with bins separated by a sequence of cutoffs

$$a = s_0 < s_1 < \dots < s_J < s_{J+1} = b.$$

Letting x_{ij} be the TIR proportion within $[s_j, s_{j+1})$ for the i th subject, $j = 0, \dots, J$, each h_i has the corresponding compositional expression $\mathbf{x}_i = (x_{i0}, \dots, x_{iJ}) \in \Delta^J$. Then, each *subsequence* $\mathbf{t} = \{t_1, \dots, t_K\}$ of the cutoffs $\mathbf{s} = \{s_1, \dots, s_J\}$, where $s_{c_j} = t_j$ with $0 = c_0 < c_1 < \dots < c_K < c_{K+1} = J + 1$, forms amalgamations:

$$\mathbf{x}_i^{(\mathbf{t})} = \left(\sum_{j=c_0+1}^{c_1} x_{ij}, \sum_{j=c_1+1}^{c_2} x_{ij}, \dots, \sum_{j=c_K+1}^{c_{K+1}} x_{ij} \right) \in \Delta^K,$$

where each component $\sum_{j=c_k+1}^{c_{k+1}} x_{ij}$ indicates the TIR proportion for the i th subject within $[t_k, t_{k+1})$, with $t_0 = a$ and $t_{K+1} = b$. We denote the amalgamated histogram corresponding to $\mathbf{x}_i^{(\mathbf{t})}$ by $h_i^{(\mathbf{t})}$.

Then, we define two types of optimality measure for thresholds \mathbf{t} for data $\mathbf{h} = \{h_1, \dots, h_n\}$, using a generic discrepancy measure between histograms $d(\cdot, \cdot)$:

1. Distribution preservation:

$$L_1(\mathbf{t}; \mathbf{h}) := \frac{1}{n} \sum_{i=1}^n d^2(h_i, h_i^{(\mathbf{t})}) \quad (1)$$

2. Distance preservation:

$$L_2(\mathbf{t}; \mathbf{h}) := \frac{2}{n(n-1)} \sum_{i < j} \left\{ d(h_i, h_j) - d(h_i^{(\mathbf{t})}, h_j^{(\mathbf{t})}) \right\}^2 \quad (2)$$

These loss functions are motivated by the dimension reduction context, thus aiming to recover the original structure of data \mathbf{h} . The first loss prioritizes preserving individual distributional information by directly minimizing the sum of discrepancies between each h_i and its amalgamated summary $h_i^{(\mathbf{t})}$. This goal aligns with classical optimal histogram binning problems for a single histogram (Knuth, 2019), while we focus on multiple histograms sharing the same thresholds. The second loss, though computationally more intensive, aims to preserve the pairwise distances between original distributions h_1, \dots, h_n . This objective is similar to multidimensional scaling (Borg and Groenen, 2007), a widely used exploratory technique in biomedical practice. Similar objectives have been used in the amalgamation of compositional data (Li et al., 2022).

Using these loss functions, we formulate the problem of selecting K optimal data-driven thresholds as the following optimization problem

$$\hat{\mathbf{t}} = \underset{\mathbf{t} \subset \mathbf{s}, |\mathbf{t}|=K}{\operatorname{argmin}} L(\mathbf{t}; \mathbf{h}), \quad (3)$$

where L is either L_1 (1) or L_2 (2), and $\mathbf{t} \subset \mathbf{s}$ indicates that \mathbf{t} is a monotonic subsequence of the high-resolution cutoffs $\mathbf{s} = \{s_1, \dots, s_J\}$. While this formulation is primarily motivated by integer-valued wearable device data—such as CGM data, where empirical distributions inherently define integer cutoffs \mathbf{s} —it extends to continuous data; see the continuous relaxation in Section 3.2.

2.1 Wasserstein distance

We propose to use the Wasserstein distance as the discrepancy measure $d(\cdot, \cdot)$ in our loss functions, which is the optimal transport metric between probability distributions (Villani, 2003). Unlike compositional distances (Aitchison, 1992) or the L^2 distance between densities, the Wasserstein distance captures the geometry of the underlying space of distribution functions and thus leverages the additional structural information encoded by histograms beyond simple compositions.

Let $\mathcal{P}(\Omega)$ denote the set of probability measures on a bounded interval $\Omega = [a, b]$ with finite second moments. The 2-Wasserstein distance d_W between two measures $\mu, \nu \in \mathcal{P}(\Omega)$ is defined as:

$$d_W^2(\mu, \nu) = \inf_{\gamma \in \Pi(\mu, \nu)} \int_{\Omega \times \Omega} |x - y|^2 d\gamma(x, y),$$

where $\Pi(\mu, \nu)$ is the set of joint distributions on $\Omega \times \Omega$ having μ and ν as marginals. The distance $d_W(\mu, \nu)$ represents the minimum “cost” of transporting mass from one distribution to another, where the cost of transporting a unit mass between points x and y is proportional to the squared Euclidean distance $|x - y|^2$ on Ω (Villani, 2003).

For one-dimensional distributions, the computation of the Wasserstein distance simplifies significantly by leveraging quantile functions. For any probability measure $\mu \in \mathcal{P}(\Omega)$, let F_μ denote

the CDF and $q_\mu(p) = \inf\{x \in \Omega : F_\mu(x) \geq p\}$ denote the quantile function. Then the 2-Wasserstein distance between μ and ν is computed as:

$$d_W^2(\mu, \nu) = \int_0^1 (q_\mu(p) - q_\nu(p))^2 dp. \quad (4)$$

2.2 Quantile piecewise linearization

The quantile-based computation of Wasserstein distance (4) offers a new perspective on the threshold selection problem within our optimization framework (3). Specifically, we further show that identifying optimal thresholds can be reframed as finding knots that yield the best piecewise linear approximations of the empirical quantile functions. Notably, the same knots are applied across all empirical quantile functions in the sample.

To illustrate this concept, Figure 1b shows a histogram h on $[40, 400]$ with six bins, separated by thresholds $s_1 < \dots < s_5$, alongside its corresponding quantile function q . The histogram is regarded as a locally constant density, having a piecewise linear quantile function shown in the right panel. In this example, we consider an amalgamation of the red adjacent bins thresholded by s_3, s_4 , and s_5 . This removes the intermediate threshold s_4 at the histogram level. At the quantile level, this operation corresponds to a *linear interpolation* between the points $(F(s_3), s_3)$ and $(F(s_5), s_5)$, where F denotes the corresponding cumulative distribution function (CDF). This interpolation is represented by the red line in the right panel.

This insight reinterprets the amalgamation-based threshold optimization framework as a problem of coarser *piecewise linearization* of quantile functions. In general, let h_1, \dots, h_n be histograms with bins separated by thresholds $\mathbf{s} = \{s_1, \dots, s_j\}$ and let $\mathbf{t} = \{t_1, \dots, t_K\}$ be a subsequence of thresholds \mathbf{s} as defined in Section 2. Denoting F_i by the CDF of each h_i , the quantile function $q_i^{(\mathbf{t})}$ of the amalgamated summary $h_i^{(\mathbf{t})}$ is constructed as a linear interpolation of the points:

$$(0, q_i(0)), (F_i(t_1), q_i \circ F_i(t_1)), \dots, (F_i(t_K), q_i \circ F_i(t_K)), (1, q_i(1)).$$

Specifically, for any $p \in (0, 1)$, let j be the index of the threshold t_j for which $p \in [F_i(t_j), F_i(t_{j+1})]$, with $F_i(t_{j+1}) \neq F_i(t_j)$. Then the piecewise linear quantile function $q_i^{(\mathbf{t})}(p)$ can be evaluated as:

$$q_i^{(\mathbf{t})}(p) = q_i \circ F_i(t_j) + \frac{q_i \circ F_i(t_{j+1}) - q_i \circ F_i(t_j)}{F_i(t_{j+1}) - F_i(t_j)}(p - F_i(t_j)). \quad (5)$$

Using these piecewise-interpolated quantile evaluations, the Wasserstein distance between distributions can be computed via the L^2 -distances between quantiles (4). We approximate the integral by evaluating the quantile functions on a grid of M equally spaced points within $(0, 1)$, denoted by $u_m = m/(M+1)$ for $m = 1, \dots, M$. A similar discretization approach for evaluating 2-Wasserstein distance has been considered in Petersen and Müller (2019); Coulter et al. (2024). The quantile values on the grid form vectors $\mathbf{q}_i = (q_i(u_1), \dots, q_i(u_M))$ and $\mathbf{q}_i^{(\mathbf{t})} = (q_i^{(\mathbf{t})}(u_1), \dots, q_i^{(\mathbf{t})}(u_M))$ in \mathbb{R}^M , leading to the following approximation of our loss functions L_1 (1) and L_2 (2):

$$L_1(\mathbf{t}; \mathbf{h}) \approx \frac{1}{n} \sum_{i=1}^n \|\mathbf{q}_i - \mathbf{q}_i^{(\mathbf{t})}\|^2 / (M+1), \quad \text{and} \quad (6)$$

$$L_2(\mathbf{t}; \mathbf{h}) \approx \frac{2}{n(n-1)} \sum_{i < j} \left\{ \|\mathbf{q}_i - \mathbf{q}_j\| - \|\mathbf{q}_i^{(\mathbf{t})} - \mathbf{q}_j^{(\mathbf{t})}\| \right\}^2 / (M+1). \quad (7)$$

Thus, the optimal thresholds $\hat{\mathbf{t}}$ in (3) correspond to the knots in piecewise linearizations of quantiles q_1, \dots, q_n that minimize the corresponding loss functions. In Section 3, we describe algorithms to solve optimization problem (3).

2.3 Semi-supervised approach

In certain cases, domain knowledge or clinical guidelines may suggest fixing some specific thresholds to maintain clinically relevant information. For instance, in CGM data, thresholds at 70 and 181 mg/dL are often critical as many clinical targets of glucose control are based on the range of 70–180 mg/dL (Battelino et al., 2019). To accommodate these needs, we propose a *semi-supervised approach* that optimizes the additional thresholds while retaining practically important thresholds.

Following the notations of (3), let $\mathbf{t}_{\text{fix}} = \{t_1^*, \dots, t_m^*\} \subset \mathbf{s}$ denote predetermined thresholds set by practitioners. We aim to identify additional thresholds $\mathbf{t}_{\text{opt}} = \{t_{m+1}, \dots, t_K\} \subset \mathbf{s} \setminus \mathbf{t}_{\text{fix}}$ that refine the amalgamations of histograms \mathbf{h} by the combined thresholds $\mathbf{t} = \mathbf{t}_{\text{opt}} \cup \mathbf{t}_{\text{fix}}$, which is sorted to compute piecewise linearizations $q_i^{(\mathbf{t})}$ (5). Using the same quantile-based loss computations L_1 (6) or L_2 (7), denoted by L , the semi-supervised optimization is formulated as:

$$\hat{\mathbf{t}} = \underset{\mathbf{t}_{\text{fix}} \subset \mathbf{t} \subset \mathbf{s}, |\mathbf{t}|=K}{L(\mathbf{t}; \mathbf{h})} \quad (8)$$

Our proposed algorithms in Section 3 accommodate the additional constraint of $\mathbf{t}_{\text{fix}} \subset \mathbf{t}$. We illustrate the semi-supervised analysis with real CGM data in Section 5, where we fix $\mathbf{t}_{\text{fix}} = \{70, 181\}$ mg/dL and identify additional optimal thresholds.

3 Algorithm

In this section, we detail algorithms for solving the threshold selection problem (3) with the quantile-based computations of optimality criteria (6) and (7). Given the challenging combinatorial nature of the problem, we consider two types of approaches: greedy stepwise algorithms and a joint optimization approach based on continuous relaxation of search space in (3).

3.1 Stepwise algorithms

The optimization (3) is a challenging combinatorial task. Given J original cutoffs $a = s_0 < s_1 < \dots < s_J < s_{J+1} = b$ and K thresholds to optimize, the problem has discrete search space of size $\binom{J}{K}$, which becomes computationally infeasible for large J and moderate K . For instance, the motivating example of CGM data with $J = 360$ and typical $K = 4$ gives over 688 million combinations. To maintain computational feasibility, we consider two iterative approaches based on merging or refining existing histogram bins: *stepwise aggregation* and *stepwise splitting*. These approaches are analogous to backward elimination and forward selection procedures for selecting the best subset of thresholds $\mathbf{s} = \{s_1, \dots, s_J\}$:

- **Stepwise Aggregation:**

1. Start with the full set of thresholds $\mathbf{t} = \mathbf{s}$.
2. Remove the threshold $s_j \in \mathbf{t}$ that minimizes $L(\mathbf{t} \setminus \{s_j\}; \mathbf{h})$, which aggregates neighboring bins of \mathbf{h} separated by s_j .

3. Iterate step 2 until the number of thresholds $|\mathbf{t}|$ reduces to K .

• **Stepwise Splitting:**

1. Start with the empty set of thresholds $\mathbf{t} = \emptyset$.
2. Add the threshold $s_j \in \mathbf{s}$ to \mathbf{t} that minimizes $L(\mathbf{t}; \mathbf{h})$, which splits an existing bin of each h_i into two parts.
3. Iterate step 2 until the number of thresholds $|\mathbf{t}|$ reaches K .

With the quantile-based computations described in Section 2.2, these stepwise algorithms can also be interpreted as iterative coarsening or refinement of piecewise linear approximations of quantile functions. Stepwise splitting is computationally more efficient for small K , whereas stepwise aggregation generally yields better solutions since thresholds are evaluated in the presence of all others; this behavior is similar to variable selection problems (Guyon and Elisseeff, 2003). We compare the empirical performance of these two approaches in Section 4.

3.2 Joint optimization with continuous relaxation

Although stepwise algorithms offer computationally feasible solutions, they may produce suboptimal results due to their local, greedy nature. To address this limitation, we also propose a joint optimization approach based on a continuous relaxation of the threshold selection problem. While our focus is on the joint optimization of histograms from integer-valued measurements, such as our motivating CGM data, the continuously relaxed formulation inherently extends our threshold optimization methodology to continuous, non-integer distributions.

The continuous relaxation arises naturally from the perspective of discretizing quantile functions described in Section 2.2. Instead of restricting thresholds for discretization to a subset of the original cutoffs $\mathbf{s} = \{s_1, \dots, s_J\}$, we allow the thresholds $\mathbf{t} = \{t_1, \dots, t_K\}$ to vary continuously across the range $\Omega = [a, b]$, subject to the monotonicity constraint $a < t_1 < \dots < t_K < b$. The linearly interpolated quantiles $q_i^{(\mathbf{t})}$ are computed as in (5). Specifically, the continuous optimization is formulated as:

$$\hat{\mathbf{t}} = \underset{\mathbf{t} \in \Omega, |\mathbf{t}|=K}{\operatorname{argmin}} L(\mathbf{t}; \mathbf{h}), \tag{9}$$

subject to the constraint $a < t_1 < \dots < t_K < b$, where L is one of the loss functions (6) or (7). The semi-supervised approach (8) similarly extends to continuous fixed thresholds $\mathbf{t}_{\text{fix}} \subset \Omega$, where the optimization follows (9) with the additional constraint $\mathbf{t}_{\text{fix}} \subset \mathbf{t}$. At the histogram level, the summarized histograms $h_i^{(\mathbf{t})}$ with continuous thresholds \mathbf{t} have compositional expressions:

$$\mathbf{x}_i^{(\mathbf{t})} = \left(\int_{t_0}^{t_1} h_i(z) dz, \int_{t_1}^{t_2} h_i(z) dz, \dots, \int_{t_K}^{t_{K+1}} h_i(z) dz \right) \in \Delta^K,$$

where h_i are regarded as locally constant densities, $t_0 = a$ and $t_{K+1} = b$. This representation generalizes amalgamation into a *soft amalgamation*, where the thresholds \mathbf{t} subdivide the original bins divided by \mathbf{s} .

The continuously relaxed problem (9) and its semi-supervised extension are nonconvex due to the dependence on the CDFs F_i in the denominators in $q_i^{(\mathbf{t})}$, as shown in (5). To solve this problem effectively, we employ *differential evolution* (DE), an evolutionary algorithm for real-valued optimization problems (Das and Suganthan, 2011). DE iteratively improves a population of candidate

solutions through mutations based on the loss function $L(\mathbf{t}; \mathbf{h})$ while being able to accommodate the monotonicity constraint involved in our problem (9). DE is particularly advantageous when the number of optimization variables is low, where it efficiently finds global or near-global optima on nonconvex landscapes. In our wearable device context, the number of thresholds K is typically small for interpretability, commonly $K = 4$ for CGM data and $K = 3$ for actigraphy summaries, as mentioned in Section 1.

For the implementation of DE, we use the `differential_evolution` function from the Python library `SciPy` (Virtanen et al., 2020). It supports incorporating the monotonicity constraint for thresholds, and other hyperparameters for initialization and mutation are set to the default values of `SciPy` for ease of implementation. Our simulation studies demonstrate that this approach consistently outperforms the stepwise approaches in loss minimization.

4 Simulations

We evaluate the performance of the proposed method on simulated data with known optimal thresholds. We consider both joint continuous optimization (9), based on differential evolution (DE), and greedy discrete optimization (3), based on stepwise aggregation (SA) and stepwise splitting (SS). For each algorithm, we consider both L_1 and L_2 losses. For comparison, we use oracle, the known optimal thresholds, and principal amalgamation analysis (PAA) (Li et al., 2022), a method from the compositional data literature. PAA optimizes the same objective as L_2 loss in (2) but uses Bray-Curtis dissimilarity as a distance measure rather than the proposed 2-Wasserstein distance. PAA solves the corresponding optimization problem using stepwise aggregation. Since PAA merges compositional variables regardless of their positions, we further impose the constraint to merge only neighboring variables to align with the histogram structures. When measuring the performance of each method, we report both estimated thresholds and the resulting value of the empirical loss. For PAA, we only report thresholds as loss values are not comparable due to the utilization of different distance measures.

To generate the data separated by K^* predefined thresholds, we consider a mixture of uniform distributions for each sample $i = 1, \dots, n$ with $n = 200$:

$$M_i := w_{i0}U_{i0} + w_{i1}U_{i1} + \dots + w_{iK^*}U_{iK^*},$$

where w_{ij} are positive weights with $\sum_j w_{ij} = 1$, and U_{ij} denotes the uniform distribution on the interval $I_{ij} = [c_{ij}, c_{i,j+1}]$, with $c_{i0} = 40$ and $c_{i,K^*+1} = 400$ the lower and upper bounds, respectively. Each M_i thus represents a histogram with thresholds c_{ij} , modeled by $c_{ij} = c_j + \varepsilon_{ij}$, $j = 1, \dots, K^*$, where $40 < c_1 < \dots < c_{K^*} < 400$ are fixed base thresholds and ε_{ij} are independent noise terms producing variability on the thresholds. In the noiseless case, the thresholds $\{c_j\}_{j=1}^{K^*}$ minimize both loss functions L_1 and L_2 evaluated with histograms M_i . Each empirical distribution \hat{M}_i is constructed from 1000 observations drawn from the mixture distribution M_i and used for comparisons. For the respective loss calculations, the oracle and DE utilize empirical quantiles of \hat{M}_i , while discrete methods (SA, SS, and PAA) first convert \hat{M}_i into histograms with 180 bins, defined by cutoffs 40, 42, \dots , 400. For oracle, DE, SA, and SS, the grid size of $M = 200$ is used for L^2 distance approximations in (6) and (7).

Throughout, we set $K^* = 3$ with base thresholds $(c_1, c_2, c_3) = (70, 180, 250)$. We draw threshold perturbation ε_{ij} i.i.d. from $N(0, \nu^2)$ with $\nu = 0, 5$, and 10, truncated to lie within $[-30, 30]$ to

Table 1: Simulation results for Setting 1 with $n = 200$. Thresholds and achieved loss values are averaged over 100 repetitions, with standard errors in parentheses. Methods compared include proposed joint optimization with differential evolution (DE), greedy methods based on stepwise aggregation (SA) and stepwise splitting (SS), and principal amalgamation analysis (PAA). Oracle refers to the base thresholds (70, 180, 250). L_2 loss values are divided by 10^3 , and bold highlights the lowest loss values for each loss function.

Noise	L_1				$L_2 (\times 10^{-3})$				PAA	
	Oracle	DE	SA	SS	Oracle	DE	SA	SS		
$\nu = 0$	t_1	70	70.2 (0.0)	70.0 (0.0)	79.9 (0.3)	70	70.5 (0.1)	70.0 (0.0)	68.6 (0.2)	70.0 (0.0)
	t_2	180	180.1 (0.1)	180.1 (0.0)	226.4 (1.2)	180	179.9 (0.1)	180.3 (0.1)	189.6 (2.0)	180.0 (0.0)
	t_3	250	251.0 (0.1)	250.1 (0.0)	251.8 (0.3)	250	252.2 (0.2)	250.3 (0.1)	259.7 (1.1)	250.0 (0.0)
	Loss	6.42 (.03)	6.35 (.03)	6.43 (.03)	71.5 (1.2)	9.93 (.16)	9.29 (.14)	10.2 (0.2)	80.8 (2.7)	–
$\nu = 5$	t_1	70	73.5 (0.1)	76.1 (0.3)	82.3 (0.3)	70	74.3 (0.2)	76.8 (0.4)	72.5 (0.4)	74.9 (0.6)
	t_2	180	179.9 (0.1)	180.3 (0.4)	227.8 (1.3)	180	178.9 (0.1)	178.9 (0.5)	187.8 (2.3)	178.5 (0.3)
	t_3	250	255.4 (0.1)	256.3 (0.5)	257.5 (0.5)	250	255.3 (0.2)	255.5 (0.5)	257.2 (1.7)	256.8 (0.5)
	Loss	17.1 (0.1)	11.5 (0.1)	15.7 (0.4)	82.3 (1.0)	29.4 (0.5)	18.8 (0.3)	28.4 (0.8)	96.4 (3.1)	–
$\nu = 10$	t_1	70	74.1 (0.1)	78.5 (0.7)	83.0 (0.2)	70	74.5 (0.2)	78.0 (0.8)	73.0 (0.4)	67.6 (0.9)
	t_2	180	178.3 (0.2)	176.6 (0.9)	229.0 (0.6)	180	177.3 (0.3)	176.3 (1.0)	186.2 (2.6)	170.7 (2.3)
	t_3	250	257.9 (0.1)	263.0 (0.8)	264.1 (0.3)	250	256.4 (0.3)	259.9 (0.9)	255.8 (8.0)	251.2 (2.1)
	Loss	32.9 (0.3)	23.6 (0.1)	37.6 (0.9)	97.1 (0.9)	60.1 (1.0)	45.1 (0.7)	74.4 (1.9)	134.4 (3.3)	–

ensure the ordering of thresholds is preserved. For the weights $\mathbf{w}_i = (w_{i0}, \dots, w_{iK^*})$, we consider two settings to explore the differences between the L_1 and L_2 loss functions:

- **Setting 1:** $\mathbf{w}_i \sim \text{Dirichlet}(20 \cdot (0.3, 0.4, 0.2, 0.1))$
- **Setting 2:** $(w_{i0}, w_{i1}) \sim 0.7 \cdot \text{Dirichlet}(5 \cdot (0.5, 0.5))$ and $(w_{i2}, w_{i3}) = (0.2, 0.1)$ [fixed]

Setting 1 represents a case where all four weights vary moderately between the samples, with optimal thresholds for both L_1 and L_2 losses expected to be (70, 180, 250). Setting 2 keeps the last two weights constant across samples while only varying the first two. Optimization with L_1 (6), which preserves the overall shape of the distributions, is expected to recover (70, 180, 250). For L_2 (7), which preserves pairwise distances, setting $K = 2$ should yield (70, 180), while $K = 3$ should include a variable 3rd threshold across replications since the region (180, 400) is non-variable across samples, making 250 non-informative for L_2 . Visualizations of the empirical quantile functions of simulated data in each setting are in Appendix A.

Table 1 presents the simulation results for Setting 1 with $K = 3$ over 100 replications. DE consistently achieves the lowest empirical loss, outperforming the empirical losses at the oracle thresholds (70, 180, 250) with similar or lower variance. SA attains empirical losses comparable to the oracle but shows higher variance under noisy conditions $\nu = 5$ and 10. SS underperforms in every scenario, with initial threshold selections clustering around 230 for L_1 loss and 190 for L_2 loss, introducing substantial bias relative to the oracle thresholds. As expected, the methods achieving smaller losses, DE and SA, closely recover oracle thresholds under both L_1 and L_2 losses. The compositional method PAA closely captures the oracle thresholds under low noise ($\nu = 0$ and 5) but becomes highly variable at $\nu = 10$, exceeding the variance observed in SA.

For Setting 2, where the last two mixture weights are fixed, the results with $K = 3$ under L_1 loss and $K = 2$ under L_2 loss and PAA are reported in Table 2. Again, DE achieves the lowest empirical losses, SA remains competitive, and SS continues to perform poorly across all scenarios.

Table 2: Simulation results for Setting 2 with $n = 200$ empirical distributions and $K = 3$ for L_1 loss and $K = 2$ for L_2 loss and PAA. Thresholds and achieved loss values are averaged over 100 repetitions, with standard errors in parentheses. Oracle thresholds are (70, 180, 250) for L_1 and (70, 180) for L_2 . L_2 loss values are divided by 10^3 , and bold highlights the lowest loss values for each loss function.

Noise		$L_1, K = 3$				$L_2 (\times 10^{-3}), K = 2$				PAA, $K = 2$
		Oracle	DE	SA	SS	Oracle	DE	SA	SS	
$\nu = 0$	t_1	70	70.1 (0.0)	70.0 (0.0)	68.0 (0.0)	70	73.2 (0.4)	70.0 (0.0)	133.2 (0.1)	70.0 (0.0)
	t_2	180	179.8 (0.1)	180.1 (0.1)	227.9 (0.3)	180	186.3 (0.8)	180.4 (0.3)	283.3 (14.3)	180.1 (0.1)
	t_3	250	250.9 (0.1)	250.0 (0.0)	252.1 (0.1)	–	–	–	–	–
	Loss	6.54 (.03)	6.46 (.03)	6.56 (.03)	39.9 (0.4)	3.71 (.05)	3.34 (.04)	3.83 (.07)	15.6 (0.2)	–
$\nu = 5$	t_1	70	74.6 (0.1)	77.7 (0.4)	74.3 (0.1)	70	76.8 (0.4)	77.9 (0.4)	132.9 (0.1)	63.8 (0.3)
	t_2	180	178.5 (0.1)	178.3 (0.5)	227.5 (0.3)	180	195.8 (1.1)	181.6 (0.8)	275.4 (16.93)	78.2 (0.3)
	t_3	250	253.9 (0.1)	254.4 (0.5)	256.9 (0.1)	–	–	–	–	–
	Loss	20.8 (0.2)	12.9 (0.1)	18.3 (0.4)	48.5 (0.5)	19.2 (0.4)	8.42 (.14)	16.1 (0.7)	25.4 (0.3)	–
$\nu = 10$	t_1	70	76.1 (0.1)	79.9 (0.8)	77.3 (0.1)	70	79.1 (0.6)	79.6 (0.8)	131.5 (0.1)	57.5 (0.4)
	t_2	180	175.1 (0.2)	173.2 (1.0)	227.1 (0.2)	180	204.7 (1.8)	172.8 (1.5)	211.0 (17.1)	81.8 (0.7)
	t_3	250	255.3 (0.1)	258.0 (0.8)	261.4 (0.2)	–	–	–	–	–
	Loss	38.5 (0.4)	26.7 (0.2)	44.1 (1.2)	66.3 (0.5)	41.4 (0.6)	24.9 (0.4)	51.8 (1.5)	53.7 (0.9)	–

As expected, the well-performing methods, DE and SA, identify thresholds close to (70, 180, 250) under the shape-preserving L_1 loss and close to (70, 180) under the distance-preserving L_2 loss. Unexpectedly, PAA deteriorates significantly under noise $\nu = 5$ and 10, though it identifies the oracle thresholds in the noiseless case. We attribute this behavior to PAA’s reliance on the Bray-Curtis dissimilarity, which ignores the geometry of the underlying domain of distributions, unlike the 2-Wasserstein distance used in SA. Figure 2 further illustrates a scenario of selecting $K = 3$ thresholds under L_2 loss for DE and SA. It shows that both DE and SA still identify thresholds near (70, 180) while finding an extra threshold unrelated to $c_3 = 250$. In a few replications, DE selects thresholds not especially close to 180, yet they reduce L_2 loss by 30-70% relative to the thresholds (70, 180, 250), suggesting that this phenomenon stems from the random generation of empirical distributions \hat{M}_i .

In summary, DE consistently optimizes thresholds with high accuracy and stability. SA performs reasonably but exhibits higher variance under noisy cases. SS consistently underperforms despite its efficiency, and PAA, while effective in noiseless scenarios, deteriorates significantly under noisy conditions. Furthermore, DE is computationally more efficient than SA and PAA under our 180-bin setting, as the stepwise procedures require $O(J^2)$ searches: SA takes 5–10 times longer than DE under both L_1 and L_2 losses, and PAA has a similar runtime to SA under L_1 . Consequently, DE stands out as the superior method for threshold optimization, providing both accuracy and computational efficiency across all examined scenarios.

5 Analysis of CGM data

In this section, we analyze datasets from two CGM studies on distinct populations. The first dataset is from a multi-center prospective study by Shah et al. (2019), which aims to establish reference glucose ranges for individuals without diabetes using modern CGM devices. The second is from a randomized, multi-center clinical trial by Brown et al. (2019), evaluating the efficacy and safety of

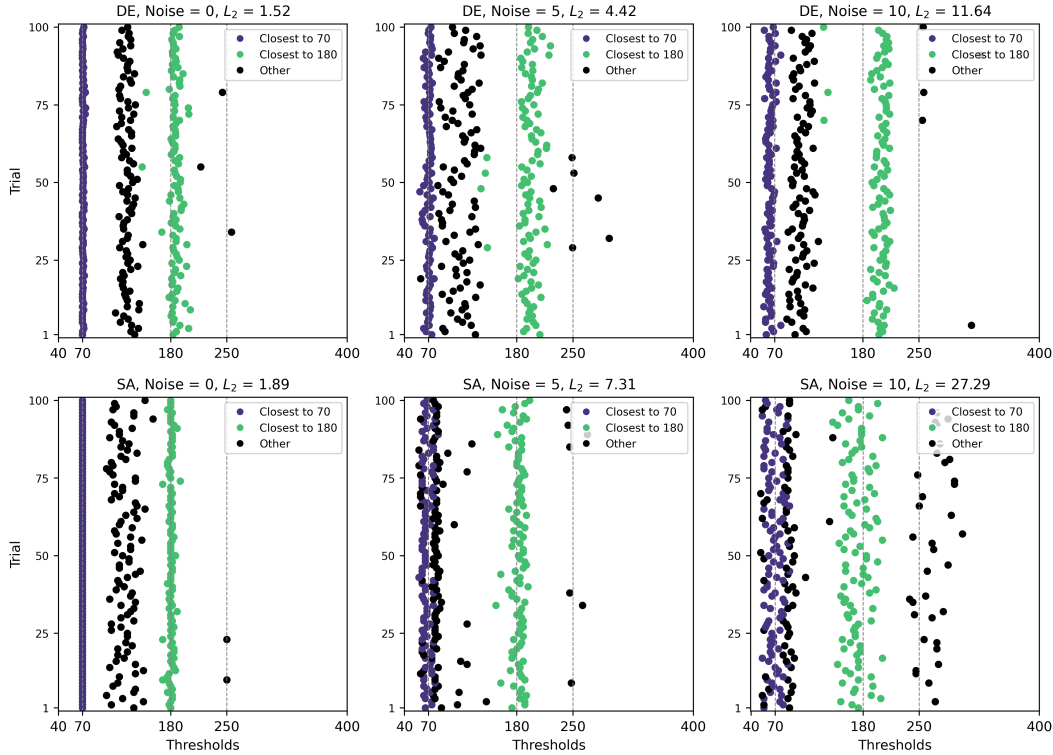


Figure 2: Results for simulation Setting 2 ($n = 200$) with L_2 loss for DE (top) and SA (bottom) under noise $\nu = 0, 5, 10$. The y -axis represents 100 replications, with obtained thresholds from each replication plotted horizontally. Vertical dashed lines indicate the base thresholds $\mathbf{c} = (70, 180, 250)$. Thresholds closest to 70 and 180 are colored in purple and green, respectively. The third threshold (black) is more variable and does not align with the base threshold $c_3 = 250$, which is non-informative for pairwise distances but informative for individual distributions. L_2 loss values are averaged and divided by 10^3 .

Control-IQ, an automated (closed-loop) insulin pump system for individuals with type 1 diabetes. Both studies employ Dexcom G6 devices recording interstitial glucose every five minutes, offering high-resolution glucose time series for each participant. We included CGM profiles if they had $\geq 90\%$ of readings for <1 day, $\geq 70\%$ for up to 2 weeks, or $\geq 70\%$ of 14 days (9.8 days) for longer periods. This led to the exclusion of 1 profile from Shah et al. (2019), resulting in 168 CGM profiles in each dataset. On average, the group without diabetes is monitored for 1.3 ± 0.4 weeks, and the group with type 1 diabetes is monitored for 28.8 ± 7.2 weeks. Both datasets are accessed from the JAEB Center for Health Research at <https://public.jaeb.org> with processing available through the Awesome-CGM repository (Xu et al., 2024).

Clinically, CGM data are commonly summarized using the consensus thresholds of 54, 70, 181, and 251 mg/dL (Battelino et al., 2023). These cutoffs define Time-in-Range (TIR) metrics, which measure the percentage of time spent in the specific glucose ranges. Time spent below 54 mg/dL or between 54 and 69 mg/dL reflects severe or mild hypoglycemia, respectively, while time between 181 and 250 mg/dL or above 250 mg/dL indicates hyperglycemia and severe hyperglycemia, respectively. Prolonged exposure to hypo- or hyperglycemia significantly increases the risk of various

health complications (Beck et al., 2018; El Malahi et al., 2022). Thus, increasing the TIR 70–180 mg/dL has become a standard clinical goal for diabetes management (Battelino et al., 2019). However, these thresholds are set primarily considering type 1 diabetes (Shah et al., 2019) and, to our knowledge, have not been assessed for optimality in a data-dependent manner. Thus, it remains unclear whether these thresholds are optimal or can be universally applied to other populations, such as individuals with type 2 diabetes or gestational diabetes.

To investigate this question, we first analyze the two datasets separately to evaluate the agreement between proposed data-driven thresholds and consensus thresholds, as well as to determine whether optimal thresholds differ between individuals with no diabetes and those with type 1 diabetes. We then combine both datasets to assess the discriminative power of data-driven thresholds versus consensus thresholds on differentiating the two populations. Specifically, we compare $K = 4$ data-driven thresholds against the full consensus set $\{54, 70, 181, 251\}$ mg/dL, and $K = 2$ thresholds against the standard TIR cutoffs $\{70, 181\}$ mg/dL. We only present results from our differential evolution (DE) approach (9) given its superior performance demonstrated in simulations, using a grid size of $M = 200$ for loss computations (6) and (7). Since CGM readings are integer-valued, non-integer thresholds identified by DE are reported after rounding up, as they equivalently summarize the CGM data.

5.1 Separate analysis

We first determine data-driven thresholds for each dataset using the L_1 loss (6), which preserves distributional shapes and is well-suited to population-wise summaries. The results with L_2 loss are qualitatively similar; see Appendix B for details.

For the data on individuals without diabetes (Shah et al., 2019), the four consensus thresholds $\{54, 70, 181, 251\}$ mg/dL yield $L_1 = 655.9$. In contrast, our DE approach with $K = 4$ attains thresholds at $\{76, 101, 124, 155\}$ mg/dL, which vastly reduces L_1 to 16.6, a 97% reduction. Figure 3 illustrates how these narrower cutoffs more accurately capture the glucose distributions of individuals without diabetes via piecewise linearized quantiles, following the perspective in Section 2.2. It also shows that the glucose readings rarely exceed 180 mg/dL, making the large consensus cutoffs of 181 and 251 mg/dL largely uninformative. Even with $K = 2$, DE finds thresholds at $\{72, 128\}$ mg/dL achieving $L_1 = 88.9$, still an 86% reduction relative to the four consensus thresholds. These data-driven thresholds reflect the typically narrower glycemic distributions of individuals without diabetes, as reported by Shah et al. (2019).

For the data on individuals with type 1 diabetes (Brown et al., 2019), the four consensus thresholds yield $L_1 = 159.9$, a smaller average discrepancy than the data on individuals without diabetes. Still, DE with $K = 4$ attains thresholds at $\{85, 172, 233, 302\}$ mg/dL, which reduces L_1 to 41.2, a 74% reduction. Notably, the first three data-driven cutoffs roughly align with the conventional 70, 181, and 251 mg/dL, while the newly identified 302 mg/dL suggests finer partitioning in the severe hyperglycemic region, which is frequently reached or exceeded in type 1 diabetes (see Figure A4 for their empirical quantiles). With $K = 2$, DE similarly finds higher thresholds at $\{211, 289\}$ mg/dL achieving $L_1 = 375.5$, a 70% reduction from the $L_1 = 1236.0$ at the standard TIR pair $\{70, 181\}$ mg/dL. These findings illustrate that higher cutoffs better capture glucose distributions for individuals with type 1 diabetes.

Despite this appeal for higher thresholds, monitoring hypoglycemia (below 70 mg/dL) or increasing the TIR of 70–180 mg/dL remains crucial for type 1 diabetes management. To address this, we also apply our semi-supervised approach (8) to the same data, fixing $t_{\text{fix}} = \{70, 181\}$

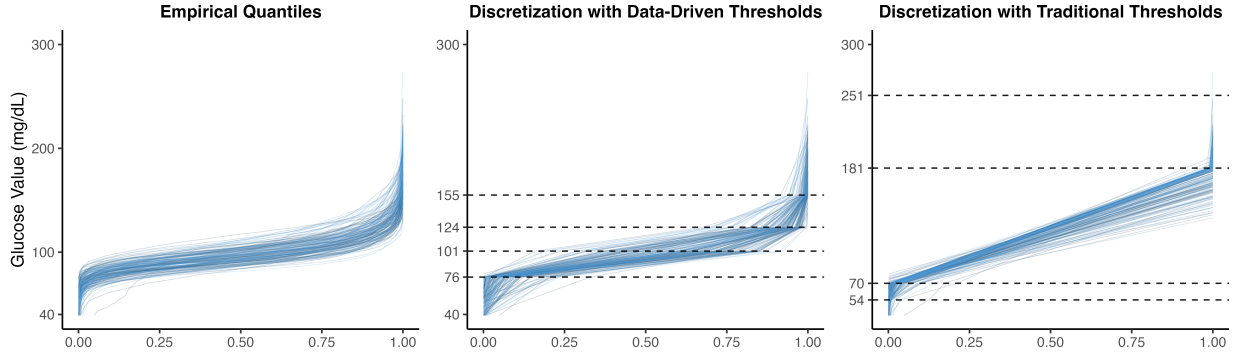


Figure 3: Quantile plots of glucose values for 168 individuals without diabetes from [Shah et al. \(2019\)](#) where each line represents a single subject. Empirical quantiles are shown in the left panel, while the middle and right panels display piecewise linearized quantiles using data-driven thresholds (L_1 loss, $K = 4$) and the traditional thresholds, respectively, with thresholds indicated by horizontal lines.

mg/dL and optimizing two additional thresholds. Under this scheme, DE identifies thresholds $\{70, 181, 241, 306\}$ mg/dL, where additional thresholds split higher glyceemic regions similarly. Although they yield a slightly higher loss $L_1 = 63.8$ than the fully data-driven solution, this still represents a 60% improvement from the four consensus thresholds. Thus, it offers more informative summaries for type 1 diabetes while preserving the standard TIR range.

Overall, these findings demonstrate that the fixed consensus thresholds $\{54, 70, 181, 251\}$ mg/dL do not optimally capture the distinct glyceemic patterns of individuals without diabetes versus those with type 1 diabetes. In contrast, our data-driven thresholds provide population-tailored thresholds, suggesting narrower cutoffs for individuals without diabetes and higher thresholds for those with type 1 diabetes. Additionally, the semi-supervised approach provides a middle ground for type 1 diabetes, preserving key clinical benchmarks while also identifying higher additional thresholds, thereby enhancing the information captured by TIR summaries.

5.2 Combined data

Next, we combine both datasets (336 total individuals) and evaluate the discriminative utility of TIR summaries using data-driven and consensus thresholds in differentiating between individuals without diabetes and those with type 1 diabetes. For this purpose, we use the L_2 loss (7), which preserves pairwise distances—an objective widely used for classifying or clustering sub-populations (the L_1 loss does not necessarily target discrimination; see Appendix B). Reported L_2 loss values are divided by 10^3 .

For conciseness, we only illustrate results with $K = 2$ thresholds, as $K = 4$ thresholds yield similar interpretations; see Appendix B. With $K = 2$ thresholds, the consensus pair $\{70, 181\}$ mg/dL yields $L_2 = 2430.0$. In contrast, DE identifies thresholds at $\{149, 256\}$ mg/dL, which reduces L_2 to 395.4, an 84% improvement. Figure 4 compares the resulting TIR summaries via compositional bar plots for both pairs of thresholds. As depicted, every interval defined by $\{149, 256\}$ mg/dL perfectly or near-perfectly discriminates the two groups: individuals with type 1 diabetes are identified by spending less than 86.7% TIR < 149 mg/dL, more than 13.7% TIR 149–255 mg/dL, and

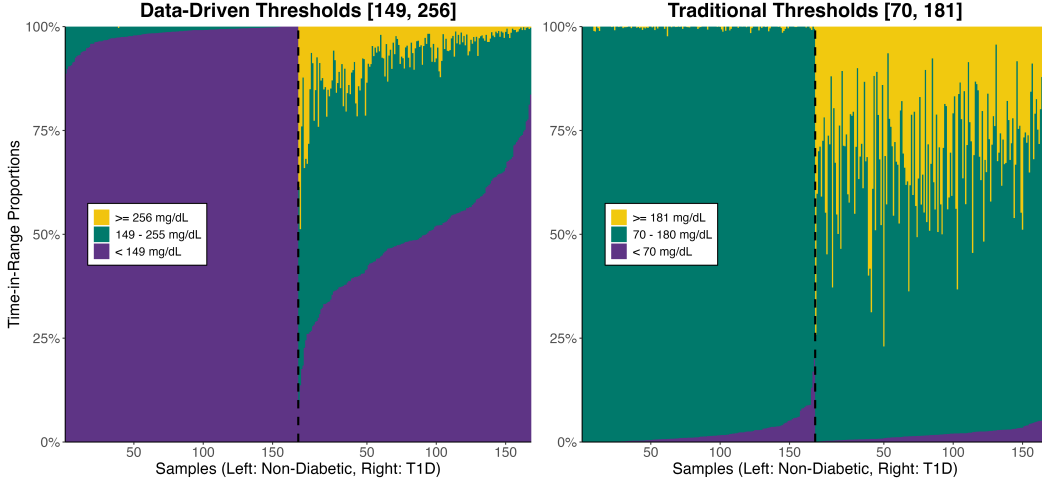


Figure 4: Compositional bar plots showing TIR proportions derived by data-driven thresholds $\{149, 256\}$ mg/dL (L_2 loss; left) and traditional thresholds $\{70, 181\}$ mg/dL (right). Individuals without diabetes and individuals with type 1 diabetes are separated by vertical black lines, with samples arranged by time below range within each group.

nonzero TIR ≥ 256 mg/dL (only one non-diabetic subject shows 0.3% TIR ≥ 256 mg/dL). In contrast, the consensus thresholds $\{70, 181\}$ mg/dL fail to discriminate the two groups via TIR < 70 mg/dL, while TIR 70–180 mg/dL achieves moderate discrimination and TIR ≥ 181 mg/dL completely differentiate the subgroups; see Table A1 for quantified classification performances with logistic regression on each TIR proportion. Consequently, our data-driven thresholds with L_2 loss demonstrate improved discrimination over the consensus thresholds, highlighting their potential for classification or clustering with interpretable TIR summaries in mixed-population studies.

6 Discussions

In this paper, we propose a new framework for data-driven thresholds to optimize wearable device data summaries, taking CGM data as our primary motivating example. By incorporating the Wasserstein distance into optimality measures, which are inspired by amalgamation in compositional data analysis, we formulate a novel perspective on threshold selection as optimal piecewise-linear approximations of quantiles. We develop two algorithmic approaches, stepwise algorithms and a joint optimization with differential evolution (DE). Simulations demonstrate the superior performance of DE, and our analyses of real CGM data reveal markedly different optimal thresholds between individuals without diabetes versus those with type 1 diabetes, illustrating potential improvements over current consensus thresholds. The semi-supervised extension allows for fixing some thresholds of practical importance, balancing domain knowledge and distributional structures.

While this paper focuses on amalgamating granular histograms of integer-valued wearable device measurements, such as CGM data, our method for optimal thresholds can also be applied to non-integer, continuous distributions via the continuous relaxation in Section 3.2. Exploring data-driven thresholds for these general distributional data presents a valuable opportunity to extract new insights through interpretable threshold-based summaries. One open question is how best to

choose the number of thresholds K . In practice, domain knowledge often suggests small K , as seen in actigraphy or CGM data, but data-driven approaches similar to PCA or clustering may also be considered. Finally, although theoretical guarantees for estimated thresholds are beyond the scope of this work, developing statistical inference methods and guarantees remains a crucial objective for future research. The Python code for implementing the proposed method is publicly available on the GitHub repository: <https://github.com/pjywang/OptiThresholds>.

Acknowledgment

The source of the [Brown et al. \(2019\)](#) and [Shah et al. \(2019\)](#) datasets is the JAEB Center for Health Research. The analyses, content, and conclusions presented herein are solely the responsibility of the authors and have not been reviewed or approved by the JAEB Center for Health Research. This research was supported by NIH R01HL172785.

References

- Aitchison, J. (1982, January). The Statistical Analysis of Compositional Data. Journal of the Royal Statistical Society: Series B (Methodological) 44(2), 139–160.
- Aitchison, J. (1992, May). On criteria for measures of compositional difference. Mathematical Geology 24(4), 365–379.
- Banker, M. and P. X. K. Song (2023, December). Supervised Learning of Physical Activity Features From Functional Accelerometer Data. IEEE Journal of Biomedical and Health Informatics 27(12), 5710–5721.
- Banker, M., L. Zhang, and P. X. K. Song (2024, December). Regularized scalar-on-function regression analysis to assess functional association of critical physical activity window with biological age. The Annals of Applied Statistics 18(4).
- Battelino, T., C. M. Alexander, S. A. Amiel, G. Arreaza-Rubin, R. W. Beck, R. M. Bergenstal, et al. (2023, January). Continuous glucose monitoring and metrics for clinical trials: an international consensus statement. The Lancet Diabetes & Endocrinology 11(1), 42–57.
- Battelino, T., T. Danne, R. M. Bergenstal, S. A. Amiel, R. Beck, T. Biester, et al. (2019, August). Clinical Targets for Continuous Glucose Monitoring Data Interpretation: Recommendations From the International Consensus on Time in Range. Diabetes Care 42(8), 1593–1603.
- Beck, R. W., R. M. Bergenstal, T. D. Riddlesworth, C. Kollman, Z. Li, A. S. Brown, and K. L. Close (2018, October). Validation of Time in Range as an Outcome Measure for Diabetes Clinical Trials. Diabetes Care 42(3), 400–405.
- Borg, I. and P. J. F. Groenen (2007, April). Modern Multidimensional Scaling: Theory and Applications. Springer Science & Business Media.
- Broll, S., J. Urbanek, D. Buchanan, E. Chun, J. Muschelli, N. M. Punjabi, and I. Gaynanova (2021). Interpreting blood GLUcose data with R package iglu. PLOS ONE 16(4), e0248560.

- Brown, S. A., B. P. Kovatchev, D. Raghinaru, J. W. Lum, B. A. Buckingham, Y. C. Kudva, et al. (2019, October). Six-Month Randomized, Multicenter Trial of Closed-Loop Control in Type 1 Diabetes. New England Journal of Medicine 381(18), 1707–1717.
- Coulter, A., R. N. Aurora, N. M. Punjabi, and I. Gaynanova (2024, March). Fast Variable Selection for Distributional Regression with Application to Continuous Glucose Monitoring Data. arXiv:2403.00922.
- Das, S. and P. N. Suganthan (2011, February). Differential Evolution: A Survey of the State-of-the-Art. IEEE Transactions on Evolutionary Computation 15(1), 4–31.
- El Malahi, A., M. Van Elsen, S. Charleer, E. Dirinck, K. Ledeganck, B. Keymeulen, et al. (2022, February). Relationship Between Time in Range, Glycemic Variability, HbA1c, and Complications in Adults With Type 1 Diabetes Mellitus. The Journal of Clinical Endocrinology & Metabolism 107(2), e570–e581.
- Fishman, E. I., J. A. Steeves, V. Zipunnikov, A. Koster, D. Berrigan, T. A. Harris, et al. (2016, July). Association between Objectively Measured Physical Activity and Mortality in NHANES. Medicine and Science in Sports and Exercise 48(7), 1303–1311.
- Freedman, D. and P. Diaconis (1981, December). On the histogram as a density estimator: L 2 theory. Zeitschrift für Wahrscheinlichkeitstheorie und Verwandte Gebiete 57(4), 453–476.
- Ghosal, R. and M. Matabuena (2024, October). Multivariate Scalar on Multidimensional Distribution Regression With Application to Modeling the Association Between Physical Activity and Cognitive Functions. Biometrical Journal 66(7), e202400042.
- Guyon, I. and A. Elisseeff (2003). An introduction to variable and feature selection. J. Mach. Learn. Res. 3(Mar), 1157–1182.
- Irpino, A. and R. Verde (2006). A New Wasserstein Based Distance for the Hierarchical Clustering of Histogram Symbolic Data. In Data Science and Classification, pp. 185–192. Springer Berlin Heidelberg.
- Janssen, I., A. E. Clarke, V. Carson, J.-P. Chaput, L. M. Giangregorio, M. E. Kho, et al. (2020, October). A systematic review of compositional data analysis studies examining associations between sleep, sedentary behaviour, and physical activity with health outcomes in adults. Applied Physiology, Nutrition, and Metabolism 45(10 (Suppl. 2)), S248–S257.
- Katta, S., H. Parikh, C. Rudin, and A. Volfovsky (2024, April). Interpretable Causal Inference for Analyzing Wearable, Sensor, and Distributional Data. In Proceedings of The 27th International Conference on Artificial Intelligence and Statistics, pp. 3340–3348. PMLR.
- Knuth, K. H. (2019, December). Optimal data-based binning for histograms and histogram-based probability density models. Digital Signal Processing 95, 102581.
- Li, Y., G. Li, and K. Chen (2022, July). Principal Amalgamation Analysis for Microbiome Data. Genes 13(7), 1139.

- Matabuena, M. and A. Petersen (2023, May). Distributional data analysis of accelerometer data from the NHANES database using nonparametric survey regression models. Journal of the Royal Statistical Society Series C: Applied Statistics 72(2), 294–313.
- Matabuena, M., A. Petersen, J. C. Vidal, and F. Gude (2021, June). Glucodensities: A new representation of glucose profiles using distributional data analysis. Statistical Methods in Medical Research 30(6), 1445–1464.
- Natali, J. M. and J. M. Pinto (2009, October). Piecewise polynomial interpolations and approximations of one-dimensional functions through mixed integer linear programming. Optimization Methods and Software 24(4-5), 783–803.
- Park, C., H. Choi, C. Delcher, Y. Wang, and Y. J. Yoon (2019). Convex clustering analysis for histogram-valued data. Biometrics 75(2), 603–612.
- Petersen, A. and H.-G. Müller (2019, April). Fréchet regression for random objects with Euclidean predictors. The Annals of Statistics 47(2), 691–719.
- Shah, V. N., S. N. DuBose, Z. Li, R. W. Beck, A. L. Peters, R. S. Weinstock, et al. (2019, October). Continuous Glucose Monitoring Profiles in Healthy Nondiabetic Participants: A Multicenter Prospective Study. The Journal of Clinical Endocrinology & Metabolism 104(10), 4356–4364.
- Troiano, R. P., D. Berrigan, K. W. Dodd, L. C. Mâsse, T. Tilert, and M. Mcdowell (2008, January). Physical Activity in the United States Measured by Accelerometer. Medicine & Science in Sports & Exercise 40(1), 181.
- Villani, C. (2003). Topics in Optimal Transportation, Volume 58. American Mathematical Soc.
- Virtanen, P., R. Gommers, T. E. Oliphant, M. Haberland, T. Reddy, D. Cournapeau, et al. (2020, March). SciPy 1.0: fundamental algorithms for scientific computing in Python. Nature Methods 17(3), 261–272.
- Xu, X., N. Kok, J. Tan, M. Martin, D. Buchanan, E. Chun, et al. (2024, December). Irinastatslab/awesome-cgm: Updated release with additional public cgm dataset and enhanced processing. <https://doi.org/10.5281/zenodo.14541646>.

Supplementary material for “Beyond fixed thresholds: optimizing summaries of wearable device data via piecewise linearization of quantile functions” by

Junyoung Park, Neo Kok, and Irina Gaynanova

Department of Biostatistics, University of Michigan, Ann Arbor, Michigan, USA

Abstract

This appendix provides additional details about the experiments. Appendix A offers supplemental information on simulation settings and additional results. Appendix B presents additional results from real-data experiments using CGM data.

A Supplementary information for simulations

A.1 Visualizations of the simulated empirical distributions

We visualize the generated empirical quantiles \hat{M}_i for simulation Settings 1 and 2 to illustrate the structures of simulated data. To simplify graphics, we depict only $n = 30$ empirical distributions under each setting with noise levels $\nu = 0, 5, \text{ and } 10$ in Figure A1. The distributions show piecewise linear patterns with vertices around the base thresholds $\mathbf{c} = (70, 180, 250)$, depicted as horizontal dashed lines. In the bottom figures on Setting 2, the variability of quantiles in the region $[180, 400]$ is tiny, representing that the pairwise distances are mostly computed along the region $[40, 180]$.

A.2 Additional simulation results

Figures A2 and A3 present additional simulation results under Setting 2 with thresholds obtained using the L_2 loss for $K = 3$ and $K = 2$, respectively. Figure A2 depicts the underperforming methods, SS and PAA, while Figure A3 includes all methods considered in the paper: DE, SA, SS, and PAA. PAA with $K = 3$ shows an interesting trend, where it often detects thresholds close to 180 even in the noisy cases of $\nu = 5$ and 10, though it also often collapses to the thresholds near 70 as in the case $K = 2$.

B Additional results for real data experiments

B.1 Separate analysis

L_2 loss results

We report the L_2 loss thresholds obtained by DE for the datasets of individuals without diabetes (Shah et al., 2019) and those with type 1 diabetes (Brown et al., 2019). L_2 loss values are reported after divided by 10^3 .

For the data from individuals without diabetes (Shah et al., 2019), DE with $K = 4$ yields thresholds at $\{77, 107, 139, 177\}$ mg/dL with $L_2 = 0.7$, a 98% reduction from $L_2 = 28.8$ at the four

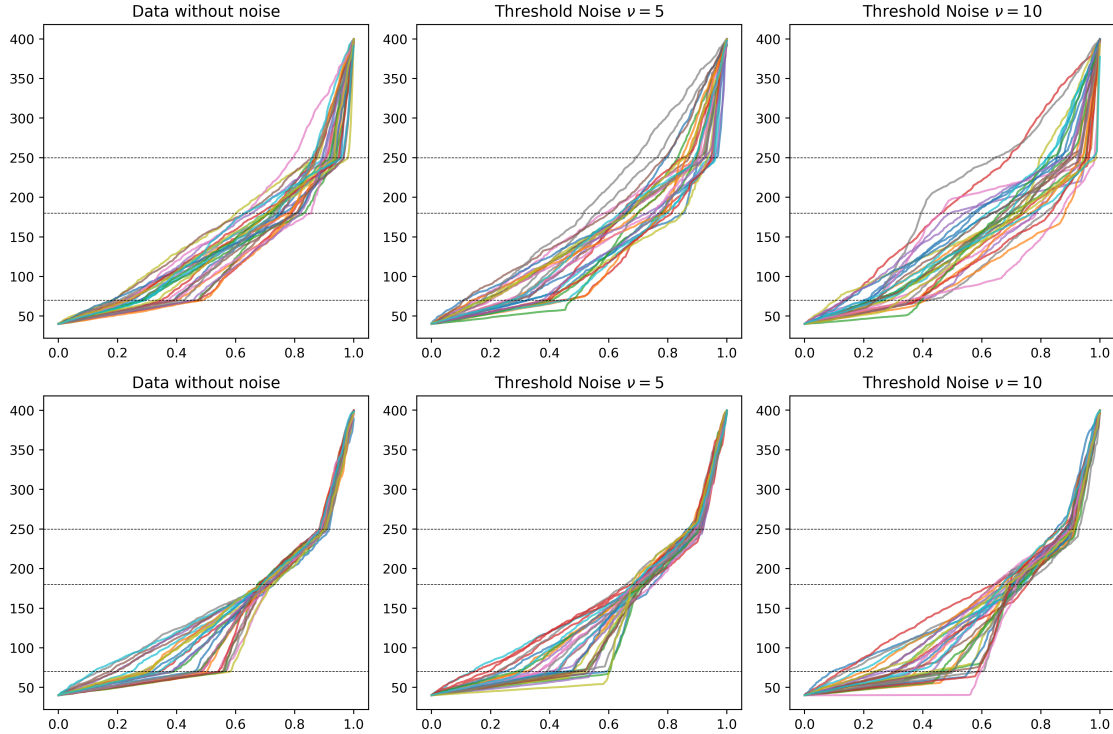


Figure A1: Visualization of the 30 empirical distributions generated for Setting 1 (top) and Setting 2 (bottom) with noise levels $\nu = 0, 5$, and 10 . Base thresholds $\mathbf{c} = (70, 180, 250)$ are shown as the dashed lines.

consensus thresholds $\{54, 70, 181, 251\}$ mg/dL. The $K = 2$ data-driven thresholds are obtained at $\{124, 164\}$ mg/dL with $L_2 = 11.6$, still outperforming the four consensus thresholds. Although different from the L_1 -derived thresholds, these L_2 -derived thresholds again suggest capturing narrower ranges for more informative summaries of CGM distributions for individuals without diabetes. Focusing on the $K = 2$ case, we also extract an interesting insight: while L_1 -derived thresholds $\{72, 128\}$ mg/dL generally capture the distributional structures, the higher L_2 -derived thresholds $\{124, 164\}$ mg/dL reveal that the higher glucose ranges are where differences in glucose distributions individuals without diabetes typically arise.

For the type 1 diabetes data (Brown et al., 2019), DE with $K = 4$ obtains thresholds at $\{169, 250, 295, 352\}$ mg/dL, which is more inflated than the L_1 -derived thresholds. These thresholds reduce the L_2 loss by 67% from the L_2 loss at the consensus thresholds. The $K = 2$ thresholds found by DE are $\{185, 285\}$ mg/dL, which still improves the L_2 loss than the four consensus thresholds by 32%. These elevated L_2 -driven thresholds indicate that differences in glucose patterns among individuals with type 1 diabetes also often arise in the higher glycemic ranges.

Quantile plot for type 1 diabetes dataset

We also provide visualizations for the dataset of individuals with type 1 diabetes (Brown et al., 2019). To further illustrate the effectiveness of the semi-supervised thresholds, we depict empirical quantiles of individuals with type 1 diabetes and their piecewise linearizations using the semi-

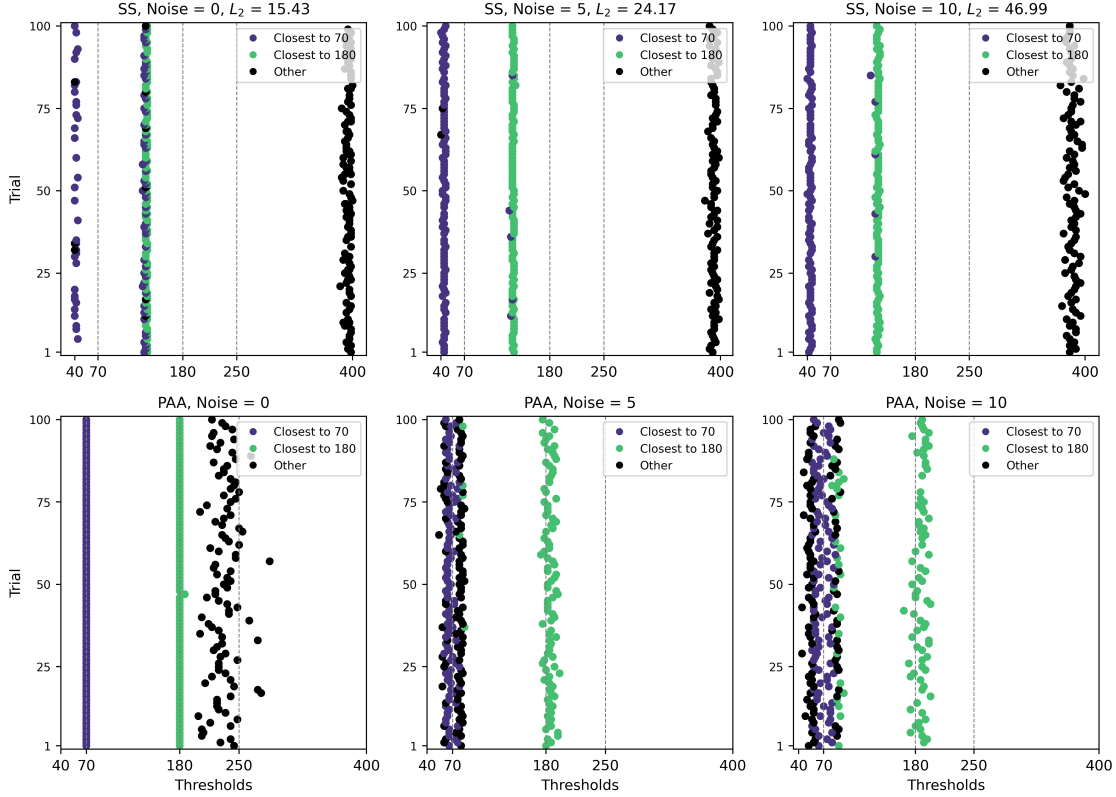


Figure A2: Simulation results under Setting 2 with $K = 3$ for PAA and SS (L_2 loss). The y -axis represents 100 replications, and the thresholds obtained in each replication are plotted horizontally. Vertical dashed lines illustrate the base thresholds $\mathbf{c} = (70, 180, 250)$. Thresholds closest to 70 and 180 are colored in purple and green, respectively. L_2 loss values are averaged and divided by 10^3 .

supervised (obtained in the real data experiment) and the consensus thresholds in Figure A4. It is observed that the semi-supervised data-driven thresholds better capture the distributional structures in the higher glycemc region than the consensus thresholds while preserving the standard thresholds $\{70, 181\}$ mg/dL for the standard TIR metric.

B.2 Combined data

Classification performance for each TIR summary

For the combined data, we first quantify the classification performance of each TIR summary illustrated in Figure 4. For this purpose, we fit univariate logistic regression on each TIR proportion defined by the data-driven thresholds $\{149, 256\}$ mg/dL and the consensus pair $\{70, 181\}$ mg/dL. The decision boundaries that optimally discriminate non-diabetic versus type 1 diabetic individuals, along with their resulting accuracies, are reported in Table A1. As the table shows, every TIR proportion defined by the data-driven thresholds achieves perfect (or near-perfect) classification. In contrast, the consensus thresholds yield suboptimal discrimination compared to our data-driven thresholds.

Table A1: Univariate logistic regression results for each TIR proportion under the data-driven (DE) thresholds {149, 256} mg/dL versus consensus thresholds {70, 181} mg/dL. ‘Decision Boundary’ is the cutoff of TIR proportion that optimally classifies non-diabetic vs. type 1 diabetic individuals. ‘Accuracy (%)’ is the classification accuracy at that boundary.

DE			Consensus		
Ranges (mg/dL)	Decision Boundary	Accuracy (%)	Ranges (mg/dL)	Decision Boundary	Accuracy (%)
TIR < 149	0.867	100.0	TIR < 70	0.020	47.0
TIR 149–255	0.137	100.0	TIR 70–180	0.893	97.9
TIR ≥ 256	0.002	99.1	TIR ≥ 181	0.033	100.0

Table A2: Univariate logistic regression results for each TIR proportion using data-driven (DE) thresholds {128, 193, 247, 312} mg/dL versus consensus thresholds {54, 70, 181, 251} mg/dL.

DE			Consensus		
Ranges (mg/dL)	Decision Boundary	Accuracy (%)	Ranges (mg/dL)	Decision Boundary	Accuracy (%)
TIR < 128	0.682	100.0	TIR < 54	0.003	60.1
TIR 128–192	0.252	98.2	TIR 54–69	0.017	47.9
TIR 193–246	0.020	100.0	TIR 70–180	0.893	97.9
TIR 247–311	0.003	99.4	TIR 181–250	0.032	100.0
TIR ≥ 312	0.000	97.9	TIR ≥ 251	0.003	99.4

$K = 4$ with L_2 loss

Next, we present experimental results with $K = 4$ thresholds. DE with L_2 loss yields thresholds at {128, 193, 247, 312} mg/dL, which improves the L_2 loss by 95% from that achieved using the four consensus thresholds. Figure A5 illustrates the compositional barplots using the data-driven and consensus thresholds. As with the case $K = 2$, the data-driven thresholds reveal clearly distinguishable differences in TIR proportions defined by them, whereas the first two TIR ranges defined by traditional thresholds, below 54 mg/dL and 54–69 mg/dL, do not capture differences between individuals without diabetes and those with type 1 diabetes. Table A2 reports the logistic regression results similarly to the $K = 2$ case, showing that our data-driven thresholds still yield almost perfect classification with these five ranges.

L_1 loss results

Finally, thresholds found by DE with the L_1 loss are presented for completeness. With $K = 2$, DE identifies thresholds at {133, 247} mg/dL, which are similar to the L_2 loss results. However, the $K = 4$ thresholds are found at {77, 124, 195, 280} mg/dL. Here, the lowest range < 77 mg/dL fails to discriminate the two groups, similar to the 70 mg/dL threshold in the standard TIR cutoffs illustrated in Table A1 (similar logistic regression accuracies using L_1 loss-derived five TIR summaries are 61.9%, 100.0%, 97.0%, 100.0%, and 98.5%, in the increasing order of the corresponding glucose ranges). Hence, although better than consensus thresholds, the TIR summaries using L_1 loss-derived thresholds do not necessarily distinguish individuals without diabetes from those with type 1 diabetes.

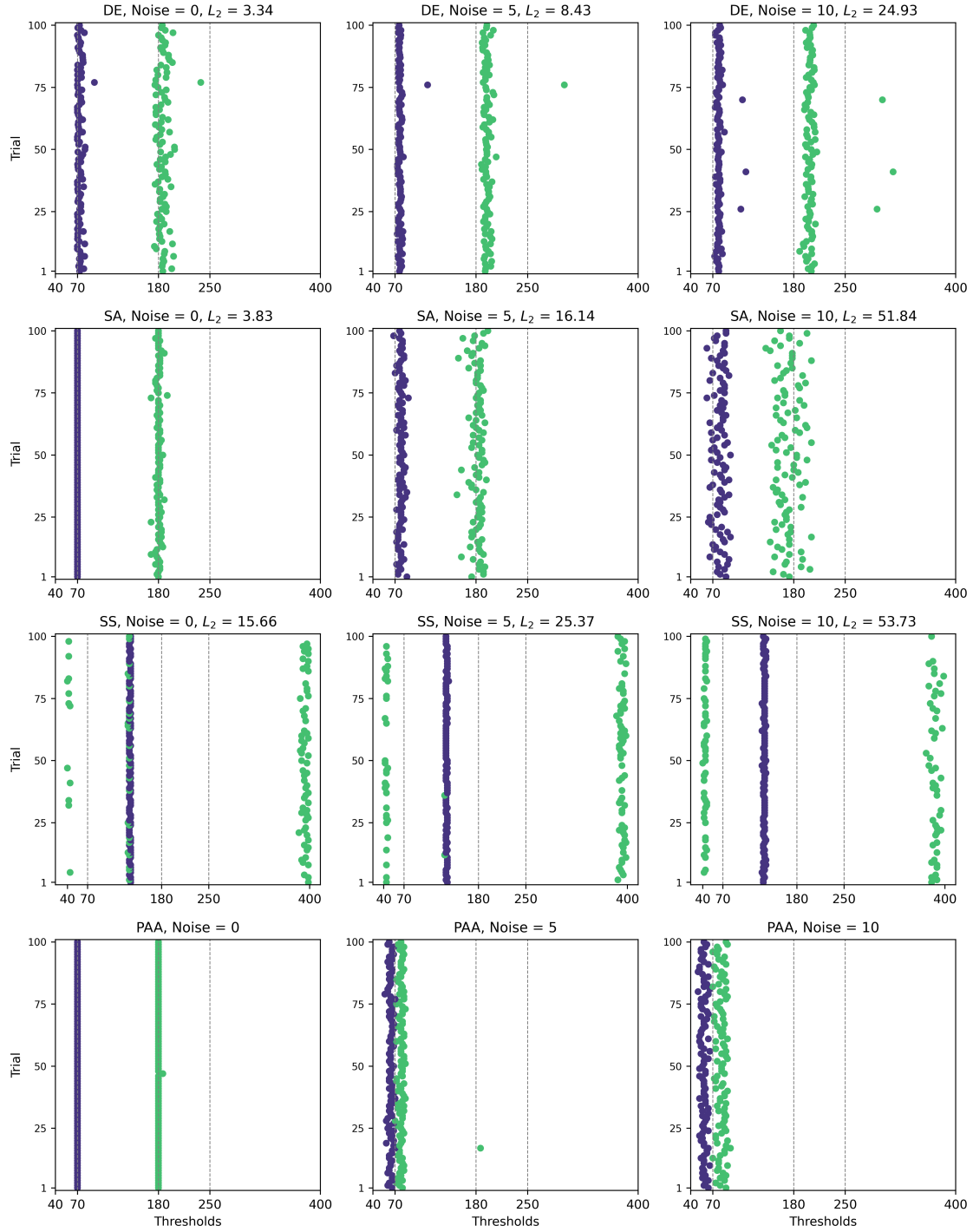


Figure A3: Simulation results under Setting 2 with $K = 2$ and L_2 loss for DE, SA, and SS, while PAA is also presented at the bottom. The y -axis represents 100 replications, and the thresholds obtained in each replication are plotted horizontally. Vertical dashed lines illustrate the base thresholds $c = (70, 180)$. Thresholds closest to 70 and 180 are colored in purple and green, respectively. L_2 loss values are averaged and divided by 10^3 .

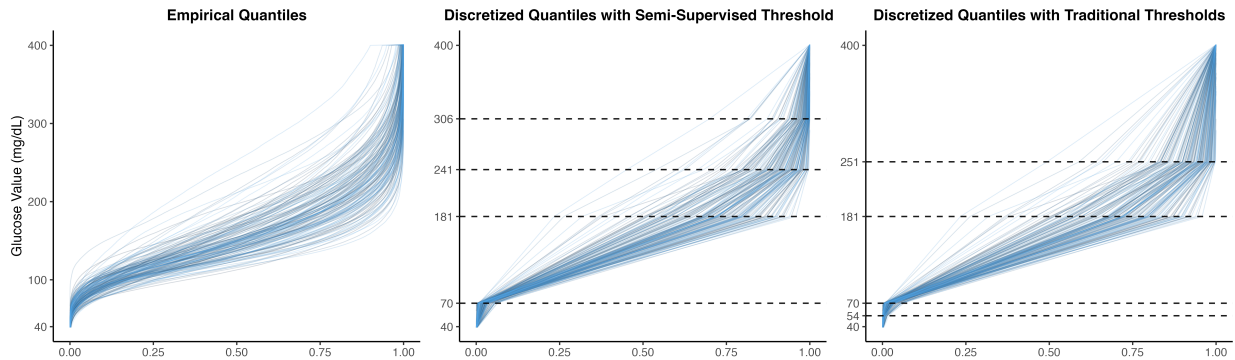


Figure A4: Quantile plots of glucose values for $n_2 = 168$ individuals with type 1 diabetes from [Brown et al. \(2019\)](#), where each line represents a single individual. Empirical quantiles are shown in the left panel, while the middle and right panels display quantiles discretized using semi-supervised thresholds (L_1 loss, $K = 4$, fixed 70 & 181 mg/dL) and traditional fixed thresholds, respectively, with thresholds indicated by horizontal lines.

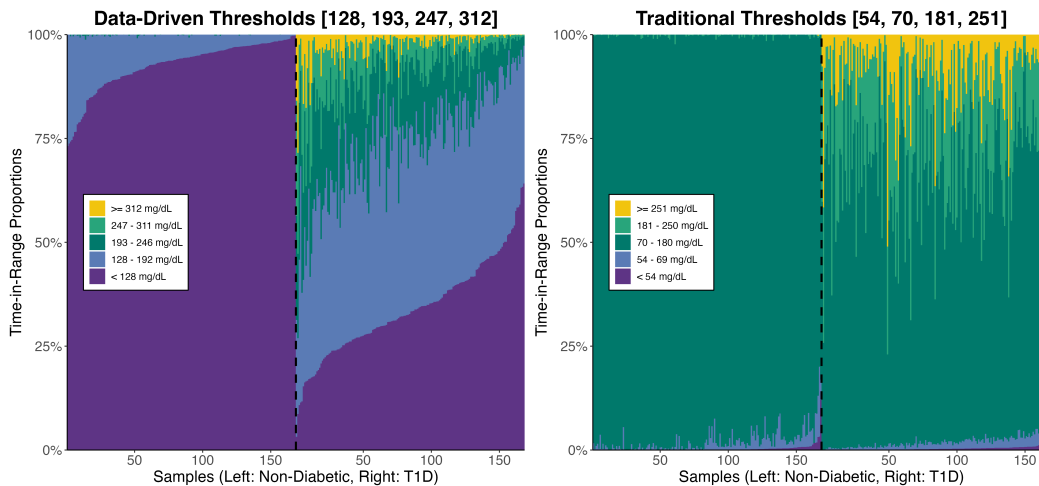


Figure A5: Compositional bar plots showing TIR proportions derived by data-driven thresholds (L_2 loss, $K = 4$; left) and traditional thresholds (right). Individuals without diabetes and those with type 1 diabetes are separated by vertical black lines, with samples arranged by time below range within each group.